Performance of Seven Land Surface Schemes in the WRFv4.3 Model for Simulating Precipitation in the Record-Breaking Meiyu Season Over the Yangtze–Huaihe River Valley in China

Zhenhua Di[1] , Shenglei Zhang[2] , Jiping Quan[3] , Qian Ma[4] , Peihua Qin[5] , and Jianduo Li[6]

[1]State Key Laboratory of Earth Surface Processes and Resource Ecology, Faculty of Geographical Science, Beijing Normal University, Beijing, China, [2]State Key Laboratory of Remote Sensing Science, Aerospace Information Research Institute, Chinese Academy of Sciences, Beijing, China, [3]Institute of Urban Meteorology, China Meteorological Administration, Beijing, China, [4]College of Global Change and Earth System Science, Beijing Normal University, Beijing, China, [5]State Key Laboratory of Numerical Modeling for Atmospheric Sciences and Geophysical Fluid Dynamics (LASG), Institute of Atmospheric Physics, Chinese Academy of Sciences, Beijing, China, [6]CMA Earth System Modeling and Prediction Centre, China Meteorological Administration, Beijing, China

Abstract In 2020, the Yangtze–Huai river valley (YHRV) experienced the highest record-breaking Meiyu season since 1961, which was mainly characterized by the longest duration of precipitation lasting from early-June to mid-July, with frequent heavy rainstorms that caused severe flooding and deaths in China. Many studies have investigated the causes of this Meiyu season and its evolution, but the accuracy of precipitation simulations has received little attention. It is important to provide more accurate precipitation forecasts to help prevent and reduce flood disasters, thereby facilitating the maintenance of a healthy and sustainable earth ecosystem. In this study, we determined the optimal scheme among seven land surface model (LSMs) schemes in the Weather Research and Forecasting model for simulating the precipitation in the Meiyu season during 2020 over the YHRV region. We also investigated the mechanisms in the different LSMs that might affect precipitation simulations in terms of water and energy cycling. The results showed that the simulated amounts of precipitation were higher under all LSMs than the observations. The main differences occurred in rainstorm areas (>12 mm/day), and the differences in low rainfall areas were not significant (<8 mm/day). Among all of the LSMs, the Simplified Simple Biosphere (SSiB) model obtained the best performance, with the lowest root mean square error and the highest correlation. The SSiB model even outperformed the Bayesian model averaging result. Finally, some factors responsible for the differences modeling results were investigated to understand the related physical mechanism.

Plain Language Summary The record-breaking precipitation that occurred in the Meiyu season during 2020 significantly affected humans and ecosystems. Can using different land surface model (LSMs) schemes affect the accuracy of precipitation simulations in numerical weather prediction models? If this is the case, how does their performance affect predictions of critical water and energy processes? In this study, we found that simulations using all of the LSMs overestimated the observations, but Simplified Simple Biosphere (SSiB) performed relatively better, with the lowest root mean square error and highest correlation. SSiB performed better than the multi-model ensemble averaging model with all seven LSMs.

1. Introduction

China experiences some of the heaviest rainstorms among the countries in East Asia. Flood disasters caused by rainstorms occur frequently every few years, and one of the areas affected most severely by floods is the Yangtze–Huaihe river valley (YHRV), where about 40% of the total flood disasters in China occur (Huang et al., 2021; Wu et al., 2021). In particular, flood disasters often occur in the Meiyu season, which usually lasts for two to 3 weeks in June and July each year.

A long Meiyu period can lead to flood disasters. In particular, the Meiyu season during 2020 in YHRV was the worst since 1961, where it was mainly characterized by the longest duration of precipitation lasting from early-June to mid-July, with frequent heavy rainstorms that caused severe flooding and deaths in China. According to statistics from the Department of Emergency Management, the floods during the record-breaking Meiyu season in 2020 affected 54.81 million people, where 158 people were dead or missing, and the affected area of crops was

5.28 million ha, resulting in direct economic losses of 144.43 billion yuan (Xinhua NEWs, 2020). Therefore, it is important to accurately predict the start and end time of the Meiyu in YHRV as well as the rainfall amounts to facilitate national flood control and disaster reduction.

Many studies have investigated the record-breaking Meiyu in YHRV during 2020 as an example to understand its causes and evolution (Chen et al., 2022; Ding et al., 2021; Liu & Ding, 2020; Qiao et al., 2021). The extreme Meiyu may have been related to the North Atlantic Oscillation, East Asian monsoon circulation oscillation, and the combined effect of Indian Ocean warming and Arctic sea ice anomalies. However, few studies have investigated the accuracy of rainfall simulation using different numerical weather prediction (NWP) models, especially in different land surface models (LSMs).

The land surface is an important and complex underlying surface at the lower boundary of the atmosphere. Physical exchanges such as those of momentum, energy, and water vapor between the land surface and atmosphere strongly influence the atmospheric circulation and climate change (Manabe, 1969). LSMs are used to describe the detailed surface characteristics and accurate exchange fluxes in order to provide a reasonable lower boundary condition for NWP models. Therefore, the accuracy of LSMs is important for the performance of NWP models. LSMs have developed in three stages from the first-generation "bucket" model to the third-generation biochemical model, but they are still affected by some uncertainties due to limitations on observations and cognition (van den Hurk et al., 2016).

Two common methods are used to improve the performance of LSMs. The first method involves developing more detailed representations of physical land processes. For instance, Friend and Kiang (2005) added descriptions of the canopy stomatal conductance and photosynthesis to a LSM, which reduced the precipitation bias by about 1 mm/day over South America. Yuan et al. (2008) implemented a groundwater dynamic model in the Regional Climate Model Version 3 (RegCM3) and found that the simulated precipitation bias was reduced by about 40% over semiarid and humid regions. The second commonly used method involves selecting an optimal LSM from numerous options. For instance, Constantinidou et al. (2020) assessed the effectiveness of four LSMs at simulating precipitation at relatively coarse horizontal resolution of 50 km by using the Weather Research and Forecasting (WRF) model over the Middle East–North Africa region, and found that Noah obtained the best performance on the overall domain, followed by its augmented version Noah-MP. Attada et al. (2018) and Reddy et al. (2020) assessed the effectiveness of three LSMs at simulating the main climatic variables such as precipitation during the Indian summer monsoon season. In addition, some uncertainty qualification methods such as parameter optimization (Li et al., 2021; Zhang et al., 2020) and ensemble forecasting (Li et al., 2017; Liu et al., 2016) have been used widely to improve the performance of LSMs.

Previous studies demonstrated that the choice of LSM can improve simulations of precipitation. However, some issues have not been addressed in previous studies. First, the number of LSMs evaluated was low (usually three to four) due to limitations on previous versions of the WRF model or a lack of computing resources (Attada et al., 2018; Constantinidou et al., 2020). At present, seven optional LSMs can be used to support simulations in the latest WRF (version 4.3). Clearly, including more LSMs in evaluations will be helpful for identifying the best at accurately simulating precipitation in the NWP model. Second, the Meiyu season is one of the main causes of flood disasters in East Asia. Many studies have evaluated the effectiveness of different LSMs in various simulations of precipitation (García-García et al., 2022; Yan et al., 2021; Zhong et al., 2021), but few have evaluated LSMs for simulating precipitation in the record-breaking Meiyu season. In the present study, we assessed seven LSMs in the latest WRF model (version 4.3) to determine the LSM that obtained the most reasonable simulations of precipitation during the Meiyu event in 2020 over the YHRV region of East China, which was the worst Meiyu event since 1961. It is important to recommend the most effective LSM for the NWP model to obtain accurate simulations of precipitation in Meiyu events in order to prevent and reduce the effects of flood disasters to maintain a healthy and sustainable ecosystem.

2. Data and Models

2.1. Precipitation Observations

Precipitation observations were obtained from China's hourly merged precipitation analysis products (CHMPA-Hourly, version 1.0), which were combined from more than 30,000 automatic weather stations in China and the Climate Precipitation Center Morphing (CMORPH) satellite precipitation remote sensing product at a
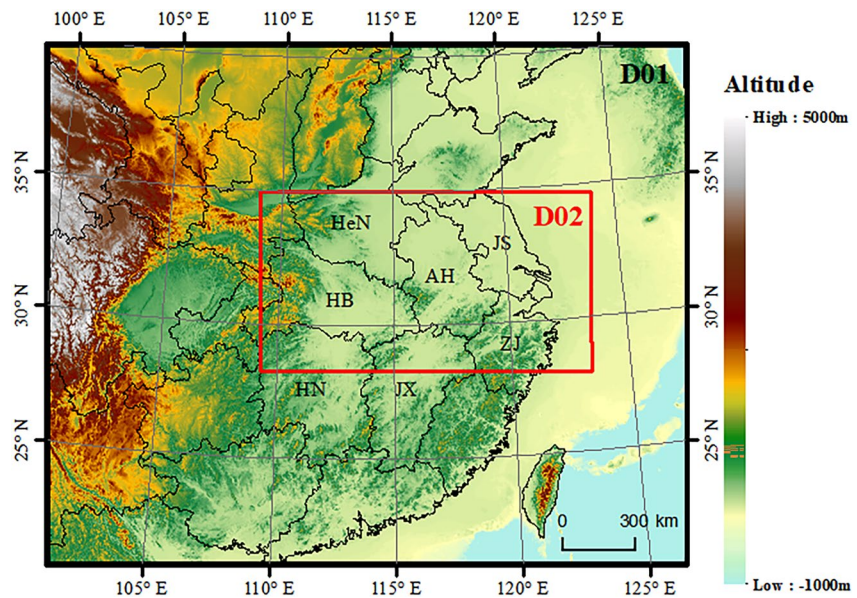
Figure 1. Weather Research and Forecasting simulation domain with double-layered nested grids, where D01 represents the outer layer region with a resolution of 27 km and the inner layer region (D02) with a resolution of 9 km. HaN, HB, and HN represent Henan, Hubei, and Hunan provinces, respectively, and JS, AH, JX, and ZJ represent Jiangsu, Anhui, Jiangxi, and Zhejiang provinces, respectively. The topography (unit: m) is also shown on the map.

horizontal resolution of 8 km covering the area between 60°S and 60°N (Shen et al., 2014). The CHMPA precipitation product has a spatial resolution of $0.1° \times 0.1°$ and temporal resolution of 1 hr. Daily precipitation data were used to avoid the influence of time deviations.

2.2. Mesoscale NWP Models and WRF Model

NWP models objectively and quantitatively forecast future weather processes by numerically solving the fluid mechanics and thermodynamics equations for processes on land, in the atmosphere, and their interactions (Pu & Kalnay, 2018). NWP models are usually implemented with supercomputers. NWP models can be divided into global and regional climate models according to differences in their spatial scale. In particular, regional climate models can obtain more accurate predictions due to their high-resolution and spatio-temporal solution of weather processes. The commonly used mesoscale NWP models mainly include PSU/NCAR mesoscale model version 5 (MM5; Chen & Dudhia, 2001), Global/Regional Assimilation and Prediction System (GRAPES; Zhong et al., 2019), and WRF (Skamarock et al., 2021). WRF is one of most widely used NWP models in previous studies.

WRF model version 4.3 (Skamarock et al., 2021; available from http://www2.mmm.ucar.edu./wrf/users) was applied to the YHRV region of China. The simulated domain comprised double-layered nested regions (Figure 1). Horizontally, the outer layer (D01) had 100×82 grid points with a grid spacing of 27 km, and the inner layer (D02) had 154×85 grid points with a grid spacing of 9 km. The inner layer D02 represented the YHRV region (109.4–123.2°E, 28.3–34.6°N). The terrain in this region is dominated by low hills and plains, and most are below 80 m above sea level. The land types mainly include paddy land, with some grassland and woodland. The land use/land cover data set required by the WRF simulation was obtained by interpolating the land use categories from United States Geological Survey 24-category data, which is applicable to all alternative LSMs in WRF. The spatial resolutions of the outer and inner layers were 10 and 2 m, respectively. Forty five uniform vertical layers were considered from the land surface to the 50 hPa level in the atmosphere. The uniform time step was 90 s. The physics options included the WSM 6-class microphysics scheme (Hong & Lim, 2006), Kain–Fritsch Eta cumulus scheme (Kain, 2004), Rapid Radiative Transfer Model (RRTM) long-wave radiation scheme (Mlawer et al., 1997), Dudhia short-wave radiation scheme (Dudhia et al., 1999), Yonsei University (YSU) planetary boundary layer scheme (Hong, 2010), and the land surface scheme (or LSM) being evaluated. This suite of physics combinations except for LSM followed the operational setup from the China Meteorological Administration.

Table 1
Main Characteristics of Slab, Noah, Rapid Update Cycle, Noah-MP, Community Land Model Version 4 Scheme, Pleim-Xiu, and Simplified Simple Biosphere Land Surface Models in the WRF

Scheme	Soil level	Soil depth (m)	Water/heat transfer between soil layers	Vegetation type in each cell	Canopy processes
Slab	5	0.31	No	Explicit vegetation effect not considered	No
Noah	4	2	Yes	One dominant vegetation type	Fixed
RUC	9	3	Yes	Specified from USGS data	Fixed
Noah-MP	4	2	Yes	One dominant vegetation type	Dynamic
CLM4	10	4.32	Yes	Four dominant vegetation types	Dynamic
Pleim-Xiu	2	1	No	Specified from USGS data	Fixed
SSiB	3	1.5	No	One dominant vegetation type	Fixed

The final analysis data (FNL) of the global forecasting system from the National Center for Environmental Prediction available at a horizontal resolution of $1° \times 1°$ and 6 hr intervals were used to generate the initial and lateral boundary conditions. The simulation period lasted 33 days from 18:00 on June 10 to 00:00 on July 13 in 2020. The first six hourly simulations were discarded as the spin-up time. Seven numerical experiments were performed by using the WRF model with seven different LSMs comprising the 5-layer thermal diffusion scheme (Slab; Dudhia, 1996), Noah scheme (Noah; Chen & Dudhia, 2001), LSM in the NOAA Rapid Update Cycle (RUC) weather prediction model (referred to as RUC in the LSM options for the WRF model; Smirnova et al., 2016), Noah multi-parameterization (MP) scheme (Noah-MP; Niu et al., 2011), Community Land Model version 4 scheme (CLM4; Oleson et al., 2010), Pleim-Xiu scheme (Pleim-Xiu; Pleim & Xiu, 1995), and Simplified Simple Biosphere scheme (SSiB; Xue et al., 1991).

2.3. LSMs

In this study, we evaluated seven LSMs available in the WRFv4.3 model comprising Slab, Noah, RUC, Noah-MP, CLM4, Pleim-Xiu, and SSiB, where their soil and vegetation features are listed in Table 1. Some of the most significant differences among these models are summarized as follows. (a) Model complexity: Slab is the simplest due to the excessive simplification of physical process descriptions, whereas CLM4 is the most complicated because of the complex parameterization formula and multiple parameters. The complexity of Noah-MP following CLM4 is due to the use of multiple optional parameterization models for each of main physical processes. The other LSMs have moderate complexity. (b) Solutions for soil moisture and temperature: the soil moisture is a simple function in the Slab model and it is related to the land use type, while the soil temperature is derived by using the thermal diffusion equation with the upper boundary of diurnal variation. The soil moisture and temperature solutions for the LSMs comprising Noah, Noah-MP, RUC, and CLM4 are based on Richard moisture transferring equation and thermal diffusion equation, respectively. In Pleim-Xiu and SSiB, the force-restore method is used to solve the soil temperature and soil moisture. The boundary conditions are also different. For instance, CLM4 takes the ground water table or gravity discharge as the lower boundary, whereas the others use a fixed value or zero flux as the lower boundary. (c) Descriptions of vegetation and snow: Slab does not consider the vegetation effect, whereas the other LSMs calculate the effects of one or more vegetation types in each calculation cell. The numbers of dominant vegetation types for each LSM are shown in Table 1. Snow cover models are considered in all of the LSMs, but their complexities are different, where Slab uses the simplest snow cover model with a fixed coverage rate, and the highly complex Community Land Model (CLM) considers a five-layer snow cover model to accurately calculate surface water and energy fluxes.

2.4. Bayesian Model Averaging (BMA)

Bayesian Model Averaging (BMA) was originally developed as a statistical post-processing method by combining multiple statistical models for joint inference and prediction. Raftery et al. (2005) extended BMA to several dynamic models. Let $f = f_1, \cdots, f_K$ represent the results of K different numerical models, y represents the

predicted quantity, and y^T represents the training data set. The BMA ensemble model can be expressed by the weighted averages of multi-model probability distributions, as follows:

$$p\big[y|\big(f_1, \cdots, f_k, y^T\big)\big] = \sum_{k=1}^{K} w_k p_k\big[y|\big(f_k, y^T\big)\big],$$

where $p_k[y|(f_k, y^T)]$ is the conditional probability density function (PDF) associated with the result of single ensemble member f_k and w_k is the posterior probability when f_k is in its optimal estimation. $w_k(k = 1, \cdots, K)$ is non-negative and constrained by $\sum_{k=1}^{K} w_k = 1$, which reflects the relative contribution of each model member to the forecasting skill for the predicted quantity y in the model training stage.

Precipitation is a non-uniform quantity, and thus its PDF is described as follows (Ji et al., 2019):

$$p_k\big[y|\big(f_k, y^T\big)\big] = p\big[y = 0|\big(f_k, y^T\big)\big]I[y = 0] + p\big[y > 0|\big(f_k, y^T\big)\big]g_k\big[y|\big(f_k, y^T\big)\big]I[y > 0],$$

where $p[y = 0|(f_k, y^T)]$ represents the PDF at zero precipitation, which is parameterized as a logistic regression model associated with the cube root of f_k, and $I[\cdot]$ is a general indicative function, with a value of 1 when the condition in [ ] is true; otherwise, the value is 0. $p[y > 0|(f_k, y^T)]$ is the PDF when precipitation occurs, and $g_k[y|(f_k, y^T)]$ is a gamma PDF.

3. Results

3.1. Spatial Comparison of Rainfall Simulations

As shown in Figure 2, the daily mean precipitation values for the Meiyu period (from June 11 to July 13 in 2020) simulated by the WRF model with different LSMs had similar spatial distributions. Overall, the amounts of precipitation simulated by all LSM models were higher than the observed values, although the patterns were similar to the observation. The four LSMs comprising Noah, RUC, CLM4, and Pleim-Xiu predicted a continuous strong rain band (Figures 2d, 2e, 2g, and 2h), whereas three other LSMs (Slab, Noah-MP, and SSiB) produced two stronger centers (Figures 2c–2f and 2i), with one in Hunan (HN) province and the other in the central and southern parts of Anhui (AH) province. Clearly, these patterns were more similar to the observations.

The biases of the spatial distributions are shown in Figure 3. No significant differences were found among the LSMs in the low rainfall areas (<8 mm/day), but significant differences were detected in the rainstorm areas (>12 mm/day). Positive bias was dominant, with one in HN province and the other mainly in the central part of AH province and the border of Jiangsu (JS) and Zhejiang (ZJ) provinces. The most significant weak bias occurred in the WRF simulation with the SSiB LSM, thereby indicating that the SSiB LSM was more advantageous for WRF simulations of precipitation during the Meiyu season in YHRV compared with the other LSMs.

Figure 4 compares the observed and simulated daily mean precipitation values for the seven LSMs in the WRF. According to the errors, no significant differences were found among Noah, RUC, Noah-MP, and CLM4 because their root mean square error (RMSE) values were about 6.8 mm/day and their correlation coefficients (CCs) were about 0.67. However, Pleim-Xiu obtained the worse performance (RMSE = 7.71 mm/day). By contrast, the Slab and SSiB LSMs performed the best among the seven LSMs, with RMSEs lower than 6 mm/day. In particular, SSiB had the lowest RMSE (5.59 mm/day) and highest CC (0.692 mm/day). Overall, the correlations among the seven LSMs were basically consistent and the main differences occurred in the error size. SSiB had the lowest RMSE and highest CC, and thus it was considered the optimal LSM in the WRF model for simulating the Meiyu season in YHRV during 2020.

3.2. Temporal Comparison of Rainfall Simulations

Figure 5 shows time series of the area-averaged daily precipitation from June 11 to July 13 in 2020 for the different LSMs. The variations in the simulated daily precipitation amounts were basically consistent for all seven LSMs. However, SSiB performed better than the other LSMs on the days with heavy precipitation compared with the observations (June 11, June 17, June 22, July 5, and July 11). On days with light precipitation, the simulation results were basically not significantly different. In general, the errors in the daily mean precipitation amounts simulated by using RUC, Noah-MP, and CLM4 were close to 5.76 mm/day, and that with Noah was slightly
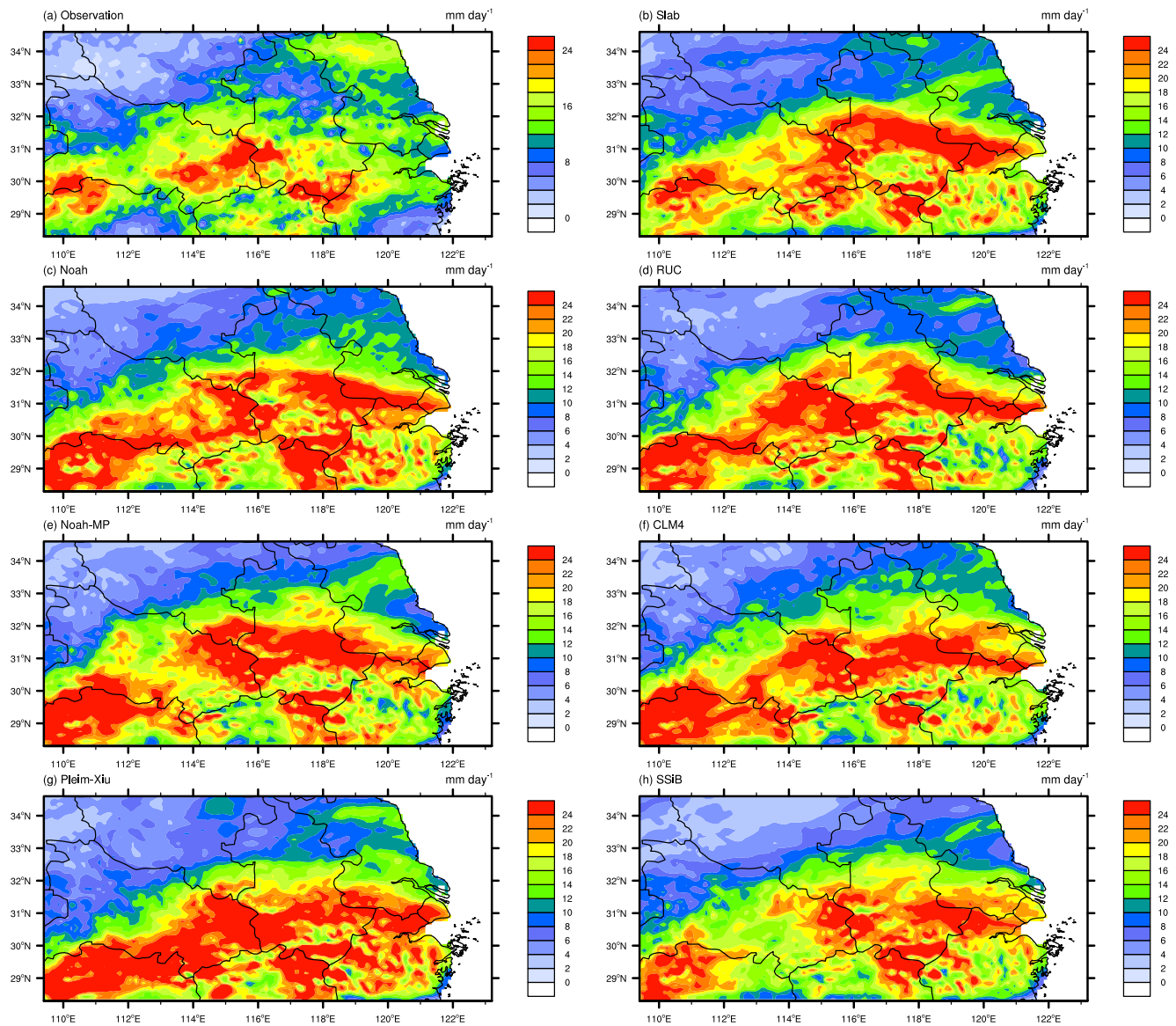
Figure 2. Spatial distributions of observed and simulated precipitation with different LSMs for the Meiyu period from June 11 to July 13 in 2020: (a) observations, (b) Slab, (c) Noah, (d) Rapid Update Cycle, (e) Noah-MP, (f) Community Land Model version 4 scheme, (g) Pleim-Xiu, and (h) Simplified Simple Biosphere.

higher at 5.95 mm/day. Pleim-Xiu had the largest error (6.10 mm/day), whereas Slab and SSiB had relatively small errors of 5.59 mm/day and 5.31 mm/day, respectively. Therefore, SSiB performed the best at simulating the daily precipitation time series.

In addition to the continuous statistical metrics (e.g., RMSE and CC), the threat score (TS) probability statistic was used to evaluate the performance of the seven LSMs. Table 2 shows the TS values for the daily precipitation simulations with each of the LSMs, including light rain (daily rainfall greater than 0.1 mm and less than 10 mm), moderate rain (daily rainfall greater than 10 mm and less than 25 mm), and heavy rain (daily rainfall greater than 25 mm and less than 50 mm). It should be noted that the TS values for storm rain (daily rainfall greater than 50 mm) were equal to zero on each day during the Meiyu in 2020, and thus, they are not listed in Table 2. Table 2 shows that Slab, RUC, and SSiB obtained higher TS values than the other models for light rain, and their TS values were basically equal. SSiB obtained significantly higher TS values than the other models for moderate rain. Thus, SSiB again performed better at precipitation simulation for the Meiyu event during 2020. It should also be noted that the TS value for SSiB was equal to zero for heavy rain, but not equal to zero for the other models. However, the TS values were basically close to zero, and only 2–4 of the 33 days had heavy rain TS
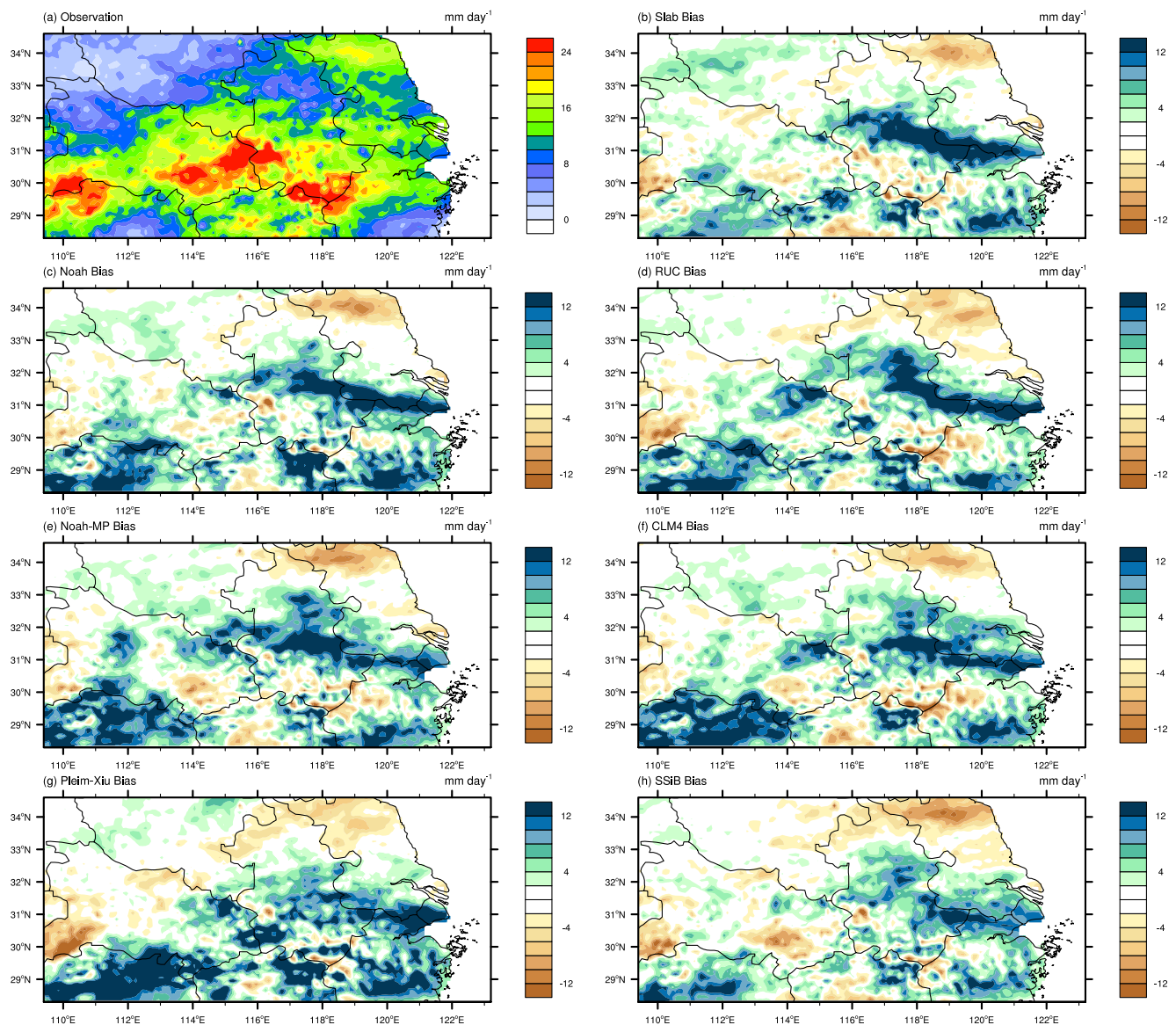
Figure 3. Spatial distributions of observed precipitation and biases of simulated precipitation (simulation–observation) with different LSMs averaged over the Meiyu period from June 11 to July 13 in 2020: (a) observations, (b) Slab, (c) Noah, (d) Rapid Update Cycle, (e) Noah-MP, (f) Community Land Model version 4 scheme, (g) Pleim-Xiu, and (h) Simplified Simple Biosphere.

values. Therefore, the comparison of the TS values for heavy rain was not representative. In addition, the spatial distribution of the precipitation was weak with SSiB, which was closer to the observations.

3.3. Comparison of Optimal Simulation and Ensemble Average Simulation

Ensemble averaging is another method for reducing model uncertainty. The seven LSMs were treated as ensemble members to conduct comprehensive uncertainty qualification analysis for the simulation results using the BMA method. Figure 6 compares the precipitation simulations using BMA and the observations. The BMA results were highly spatially consistent with the observations, but the optimal LSM comprising SSiB had stronger correlations than BMA.

Further comparisons were also conducted to represent the differences in the LSMs more accurately. Figure 7 shows scatter plots of the precipitation simulation with BMA versus the observations and precipitation simulation with the optimal LSM versus the observations. BMA obtained relatively good performance compared with the observations, but SSiB performed better than BMA in terms of RMSE and CC. In particular, the CC for precipitation simulation with SSiB was 0.73, which was higher than that for the BMA simulation (0.69). Similarly, the RMSE
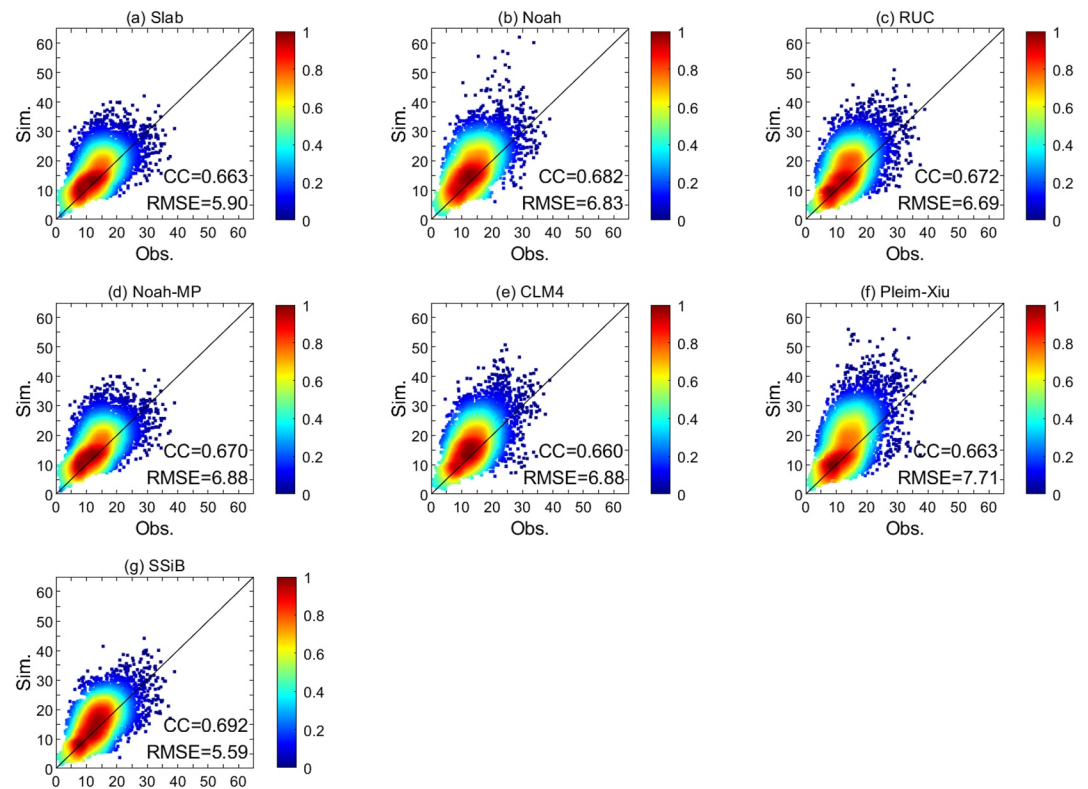
Figure 4. Simulated daily mean precipitation values (*y*-axis, mm/day) versus observed values (*x*-axis, mm/day): (a) Slab, (b) Noah, (c) Rapid Update Cycle, (d) Noah-MP, (e) Community Land Model version 4 scheme, (f) Pleim-Xiu, and (g) Simplified Simple Biosphere.
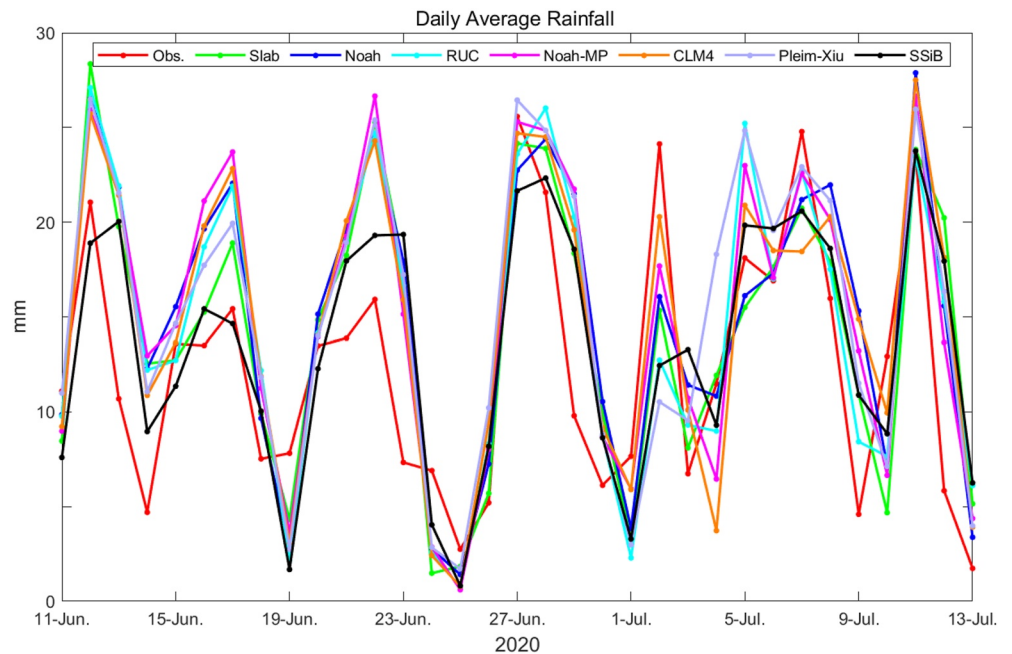

Figure 5. Time series of area-averaged daily accumulated precipitation amounts in simulations using seven LSMs and observations.

Table 2

Threat Score (TS) Statistics for Daily Precipitation Simulations Using Different LSMs Over the Meiyu Event in Yangtze–Huai River Valley During 2020

	Light rain (mm/ day) [0.1, 10)	Moderate rain(mm/ day) [10, 25)	Heavy rain (mm/ day) [25, 50)
Slab	0.1156	0.0901	0.0101
Noah	0.0966	0.0970	0.0115
RUC	0.1188	0.0883	0.0120
Noah-MP	0.1019	0.0810	0.0208
CLM4	0.1019	0.0941	0.0115
Pleim-Xiu	0.0759	0.0919	0.0208
SSiB	0.1150	0.1015	0

for the precipitation simulation with SSiB was 5.59 mm/day, which was significantly lower than that for the BMA simulation (6.0 mm/day). In addition, the improvement in the precipitation simulation results with BMA for each LSM ranged from 10.3% for RUC to 22.2% for Pleim-Xiu. Clearly, BMA integrated the advantages of each ensemble member to help obtain greater performance than each separate LSM to effectively reduce the uncertainties associated with each model and between the models.

4. Discussion

4.1. Comparisons With Similar Studies

Many studies have evaluated the differences in the performance of LSMs in terms of precipitation, and they mainly used Noah, Noah-MP, CLM4, and Pleim-Xiu. For instance, Zhong et al. (2021) found that Noah-MP obtained the optimal simulation of precipitation compared with CLM4 and Pleim-Xiu in the Tibetan Plateau region. After analyzing the mechanism responsible
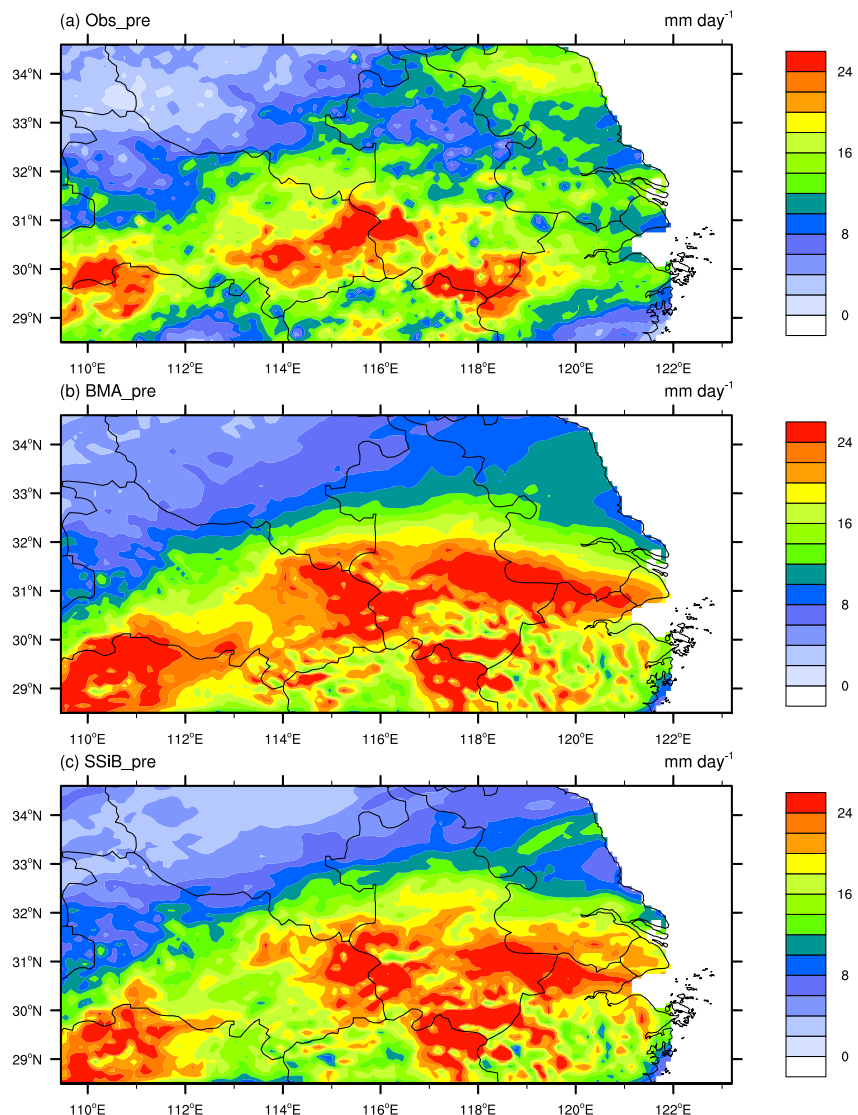

Figure 6. Comparison of precipitation simulations using Bayesian Model Averaging with the seven LSMs and the optimal LSM comprising Simplified Simple Biosphere.
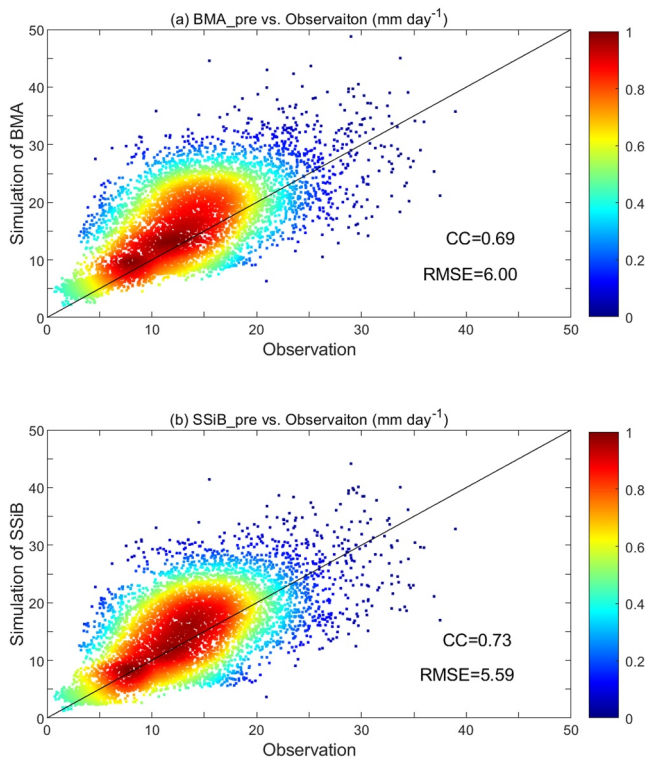
Figure 7. Scatter plots for precipitation simulation using Bayesian Model Averaging versus observations (top) and precipitation simulation with the optimal scheme versus observations (bottom).

for the differences, they found that the drier soil moisture conditions and lower latent heat flux produced by Noah-MP constrained the wet bias in the precipitation simulation, so the results were closer to the observations compared with the other two LSMs. Similar conclusions were obtained based on precipitation simulations over North America by Chen et al. (2014) and García-García et al. (2022). Zhuo et al. (2019) found that three LSMs comprising Noah, Noah-MP, and CLM4 basically obtained consistent performance in Northern Italy, and we also produced similar results in our study. In addition, Slab performed better than other LSMs comprising Noah, RUC, and Pleim-Xiu in simulations of storms in the YHRV region over China (Wang et al., 2016; Zeng et al., 2012). These differences in performance may be related to the different surface energy flux distributions produced by different LSMs. Thus, the decreased latent heat flux with Slab could have resulted in a low contribution of evapotranspiration (ET) to precipitation, which reduced the occurrence of high precipitation situations in LSM simulation. We found that Noah-MP and Slab performed well at simulating precipitation, but SSiB performed the best in the YHRV region of China. In previous studies, SSiB also performed better in precipitation simulations over East Asia (Li et al., 2016) and South Asia (Lu & Zuo, 2021), although these studies focused on low resolution climate simulations (∼50 km) rather than Meiyu seasons, and only four LSMs were considered (Noah, CLM, Pleim-Xiu, and SSiB).

4.2. Surface Water Vapor Flux

Land surface processes affect precipitation via two routes in terms of the water balance (Zeng et al., 2011), that is, by directly affecting the surface ET flux to produce precipitation and influencing precipitation by changing the low-level wind circulation and moisture flux convergence. Table 3 summarizes the daily area-averaged amounts of ET and precipitation simulated by the seven LSMs for the YHRV region. ET accounted for 16%–23% of the rainfall, thereby demonstrating that moisture flux convergence was still the dominant factor that affected precipitation. ET increased as the rainfall increased. In addition, the proportion of ET relative to rainfall differed among the LSMs. For instance, the ET was smallest with Slab, while that under Noah was close to those under Noah-MP and CLM4, and it was largest with Pleim-Xiu. These different proportions demonstrate that precipitation simulations in WRF are sensitive to the choice of LSM.

Table 3 shows that Slab obtained the smallest simulated ET and precipitation amounts among the seven LSMs. Compared with Slab, the increases in ET were more than half of the increases in rainfall with five other models (Noah, RUC, Noah-MP, CLM4, and Pleim-Xiu). Thus, the differences in rainfall caused by these LSMs were mainly due to differences in ET. By contrast, the rainfall simulated by SSiB decreased as the ET increased. Thus, SSiB contributed less to water vapor convergence than Slab. Table 3 shows that the percentage of ET relative to rainfall was higher under SSiB than Slab, and thus, less moisture flux convergence occurred with SSiB according to the water balance principle, and the SSiB results were closer to the observations. Clearly, the ET/rainfall of no more than 23% demonstrated that moisture flux convergence was still the dominant factor that affected precipitation.

Table 3
Daily Area-Averaged Evapotranspiration (ET) and Precipitation Amounts Simulated by the Seven LSMs for the Yangtze–Huai River Valley Region During the Meiyu Period

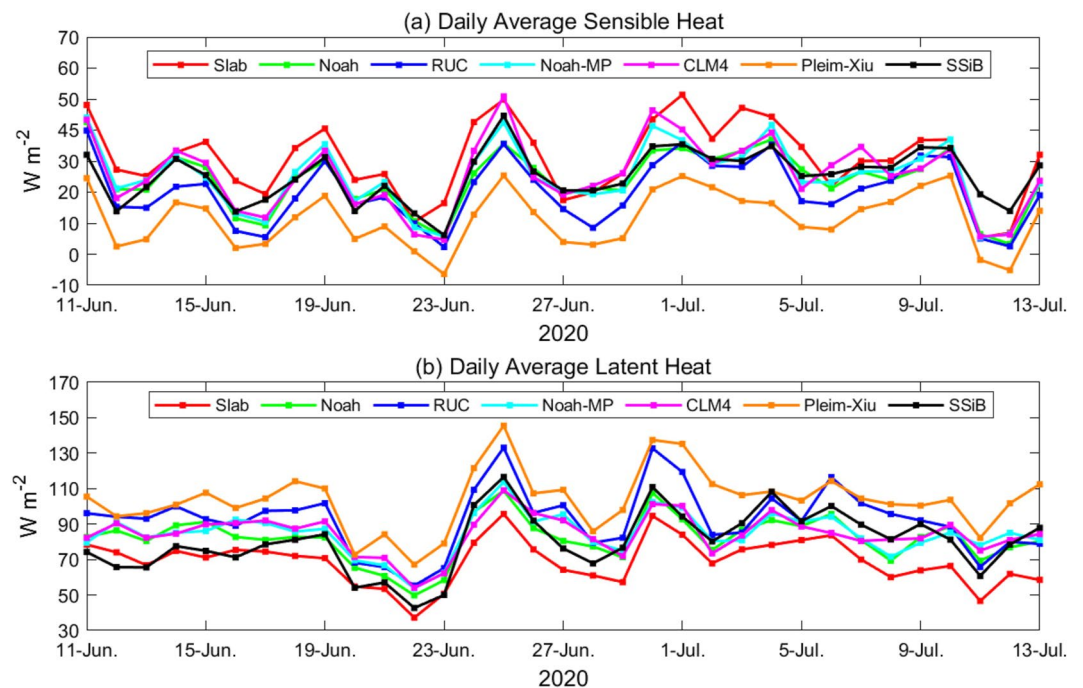|	Slab	Noah	RUC	Noah-MP	CLM4	Pleim-Xiu	SSiB
ET (mm/day)	2.44	2.89	3.26	2.98	2.98	3.66	2.83
Rainfall (mm/day)	14.93	15.81	15.31	15.78	15.75	16.10	14.10
ET/Rainfall	16.31%	18.27%	21.31%	18.90%	18.95%	22.74%	20.09%

Figure 8. Time series of area-averaged daily heat fluxes obtained from simulations using the seven LSMs: (a) sensible heat flux and (b) latent heat flux.

4.3. Surface Energy Flux

The choice of LSM directly affects the simulated surface energy flux. Figure 8 shows the simulated area-averaged daily heat fluxes comprising the sensible heat and latent heat fluxes for the WRF model with different LSMs over the Meiyu period from June 11 to July 13 in 2020. Both the sensible and latent heat fluxes varied under the different LSMs. In general, the sensible heat flux decreased in the order of: Slab > CLM4 > SSiB > Noah-MP > Noah > RUC > Pleim-Xiu, whereas the latent heat flux increased accord- ing to the same sequence. Among the LSMs, the heat fluxes for Slab, Pleim-Xiu, and RUC were significantly different from those with the other LSMs. For example, the sensible heat flux was the smallest with Pleim-Xiu and the latent heat flux was the largest, with a difference of up to 92 W/m^2, and the difference with RUC was up to 70 W/m^2. Slab obtained the lowest difference of 40 W/m^2. The sensible heat fluxes with Noah, Noah-MP, CLM4, and SSiB were 23–25 W/m^2, and latent sensible heat fluxes were 80–84 W/m^2, and thus the difference in the two fluxes were about 60 W/m^2. The approximate flux simulation results may have been responsible for the consistent differences in the precipitation simulation results (Figure 4). In addition, with all of the LSMs, the simulated sensible heat fluxes ranged from 11.37 W/m^2 to 30.74 W/m^2 and the simulated latent heat fluxes ranged from 60.09 W/m^2 to 103.86 W/m^2. These findings also demonstrate that selecting different LSMs will lead to large differences in the simulated surface energy flux allocations.

The latent heat flux is significantly affected by ET and soil moisture. Zhong et al. (2021) found that higher soil moisture increased the latent heat flux, and thus the atmospheric water content and moist static energy were greater in the planetary boundary layer to ultimately increase the frequency and intensity of precipitation. We also found that the latent heat flux was basically consistent with the average simulated rainfall. For instance, the latent heat fluxes were relatively small with Slab and SSiB (Figure 8b), thereby resulting in relatively small simulated precipitation and ET amounts with all seven LSMs (Figure 2 and Table 3), and thus, the simulated results were closer to the observations.

Figure 9 shows the spatial distributions of the simulated latent heat flux averaged over the Meiyu period with the different LSMs. Except for Slab, the latent heat fluxes simulated by the other LSMs tended to increase from north to south, which was consistent with the observed precipitation pattern. Overall, Slab obtained the smallest heat flux. Noah, Noah-MP, and CLM4 produced similar latent heat flux distributions, and their precipitation errors were also similar (Figure 4), thereby indicating that Noah, Noah-MP, and CLM4 simulate precipitation
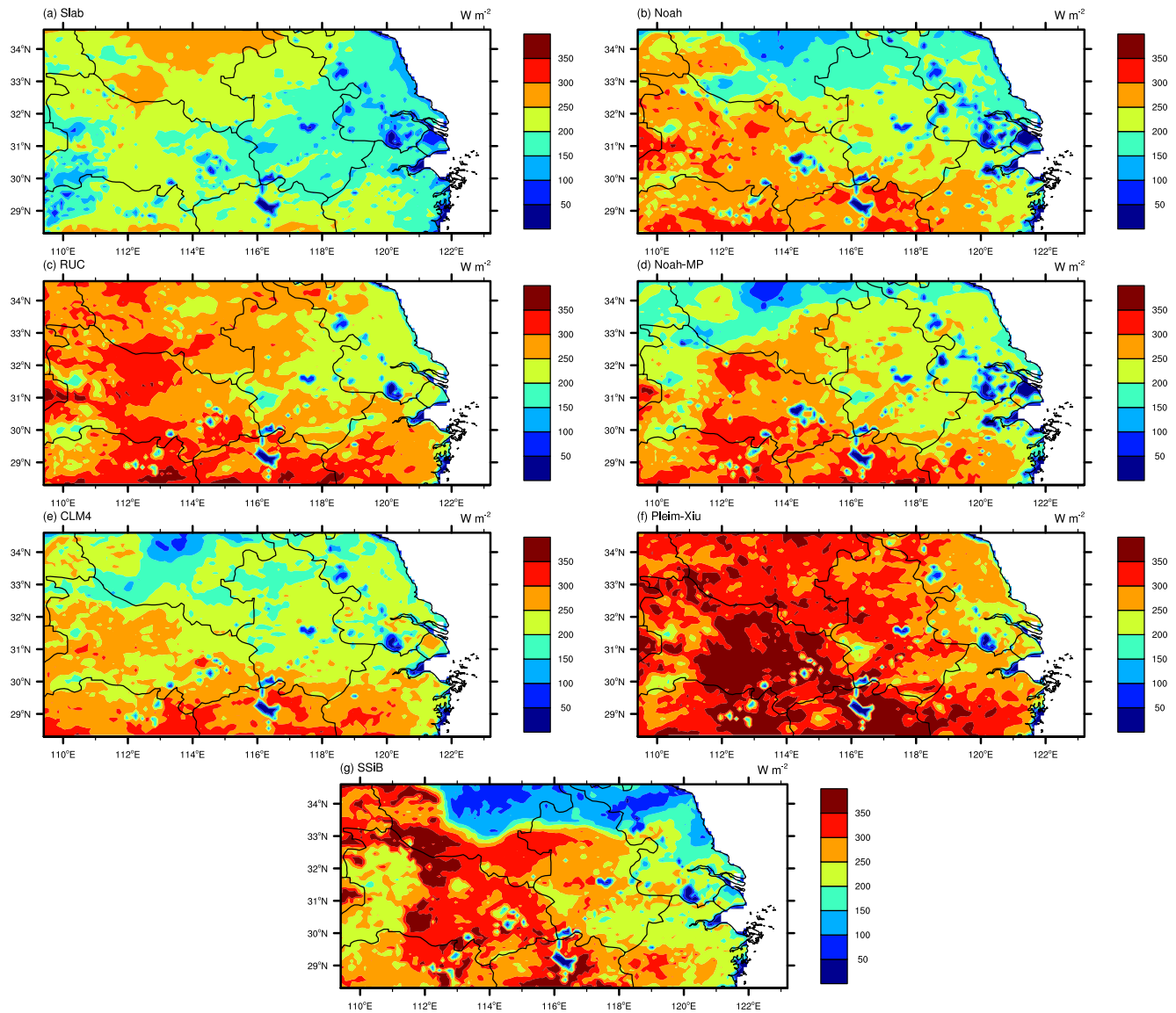
Figure 9. Spatial distributions of the simulated latent heat fluxes averaged over the Meiyu period from June 11 to July 13 in 2020: (a) Slab, (b) Noah, (c) Rapid Update Cycle, (d) Noah-MP, (e) Community Land Model version 4 scheme, (f) Pleim-Xiu, and (g) Simplified Simple Biosphere.

with a similar mechanism. In addition, the simulated latent heat flux distributions were stronger with RUC and Pleim-Xiu than SSiB, which corresponded to their different precipitation distributions. Therefore, the difference in the latent heat flux (or ET) was one of the major causes of the different precipitation spatial distributions in the Meiyu event.

4.4. 850 hPa Geopotential Height Fields, Wind, and Moisture Flux Convergence

The 850 hPa geopotential height field can reflect the water vapor convergence and divergence, and thus, it was analyzed as an indicator of precipitation forecasts (Shirvani et al., 2019). Figure 10 shows the simulations of the 850 hPa geopotential heights for the seven LSMs. The simulated low-pressure center in the west of the 850 hPa geopotential height field differed significantly among the LSMs, which corresponded well with their simulated heavy precipitation centers (Figure 2). For instance, the low-pressure centers with Noah, RUC, Noah-MP, and Pleim-Xiu stretched from the southwest to northeast and formed a continuous rain band. However, the low-pressure (1,440 gpm) center zones with Slab and SSiB were in the southwest, forming a southwest precipitation center, which corresponded well with the observed precipitation center.
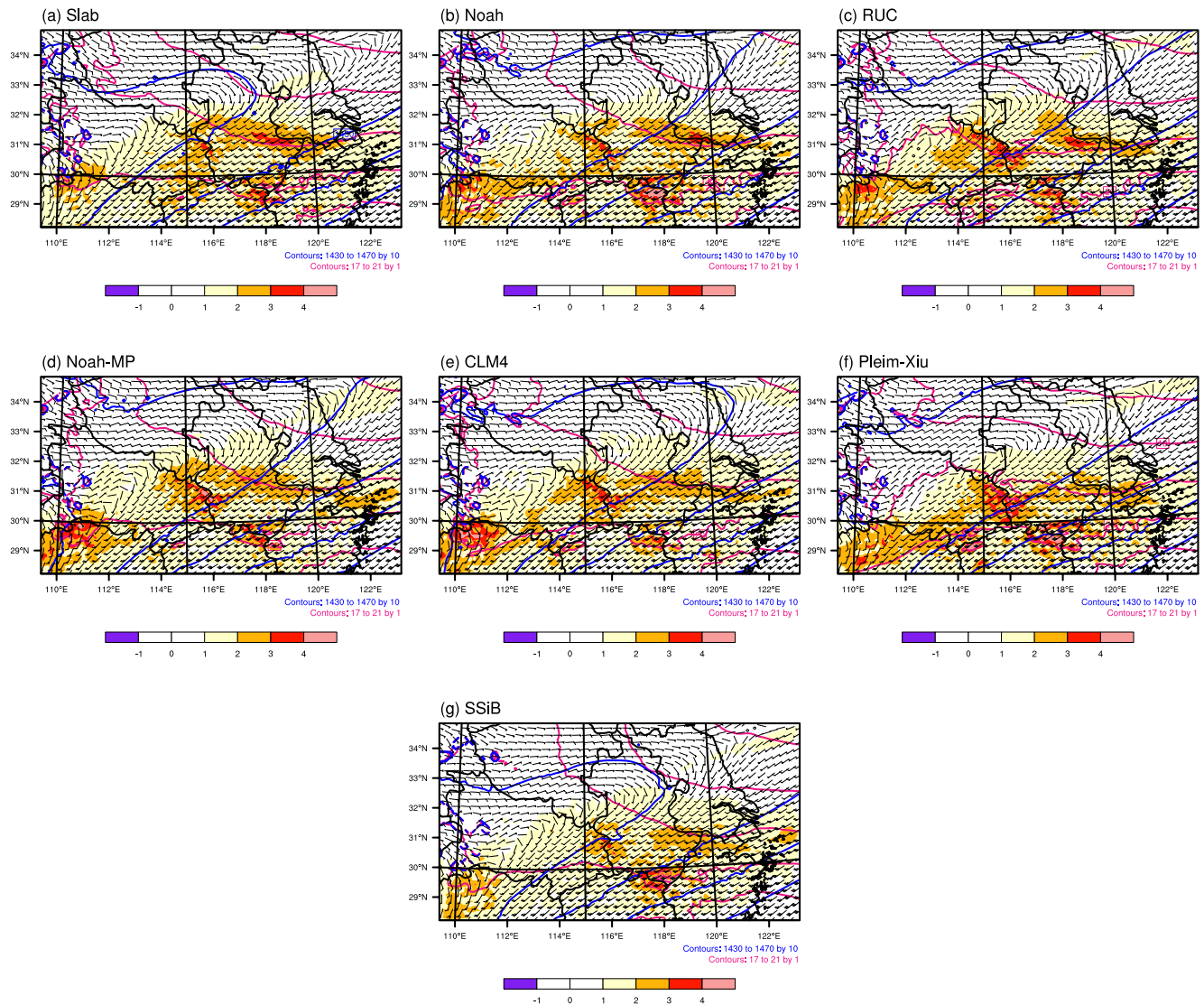
Figure 10. Fields of daily mean geopotential height (unit: gpm, blue contour lines), wind (unit: m/s, gray vectors), and temperature (unit: °C, pink contour lines) at 850 hPa, and integrated moisture flux convergence (unit: mm/day, contour shade) over the Meiyu period from June 11 to July 13 in 2020: (a) Slab, (b) Noah, (c) Rapid Update Cycle, (d) Noah-MP, (e) Community Land Model version 4 scheme, (f) Pleim-Xiu, and (g) Simplified Simple Biosphere.

Under the influence of the summer monsoon, the prevailing southwest wind brings abundant warm and moist water vapor to the area simulated in this study. The water vapor convergence area mainly formed in the southwest corner of the simulated area and the central and southern part of Anhui province. Figure 10 illustrates the integrated moisture flux convergence (Tsuji et al., 2021). Compared with the spatial rainfall diagram (Figure 2), the area with stronger moisture flux convergence (>2 mm/day) corresponded to the stronger rainfall area, thereby indicating that the precipitation in this area was contributed mainly by moisture flux convergence. In addition, the moisture flux convergence was smallest with SSiB, which corresponded to the low rainfall distribution (Figure 2h), and Table 3 also shows that the increased ET with SSiB led to decreased precipitation.

4.5. Critical LSMs Parameters That Affected Precipitation Simulations

The parameter settings are the main factors that affect the simulation results obtained by different LSMs. In order to ensure objectivity and fairness, the default parameters were used for each of the LSMs evaluated in this study without artificial parameter adjustment. Similarly, for the Noah-MP model with alternative multi-schemes, the default parameterization option was adopted for each physics. The critical LSM parameters that affected

the precipitation simulation performance are summarized as follows. (a) The soil hydraulic conductivity affects the conduction velocity of soil water between the soil upper and lower layers. When the soil hydraulic conductivity increases, soil water will be transferred faster in the soil layer. The rainfall amount is affected when more soil water is transferred to the ground surface to participate in surface evapotranspiration. (b) The soil thermal conductivity determines the soil heat conduction velocity between the upper and lower layers in a similar manner to the soil hydraulic conductivity. Finally, the surface soil temperature is affected by the soil thermal conductivity to influence the surface evapotranspiration and further affect the rainfall amount. (c) The scale factor between actual and potential ET determines how well the simulated ET agrees with the observed value. The scale factor is a power function for the soil moisture in CLM4 and SSiB and a linear function for the soil moisture in Noah and Noah-MP. Xiao et al. (2017) found that the power parameterization in CLM and SSiB performed better than the linear parameterization in Noah. (d) Other parameters. For example, soil parameters such as the number of soil layers and soil depth, snow cover parameters such as the number of snow layers, snow albedo, and snow duration, and vegetation parameters such as the vegetation fraction, minimum stomatal resistance, and roughness length can also affect the performance of different LSMs to some extent.

4.6. Effects of Different LSM Rainfall Accuracies on Public Health Evaluations

The relationships between the improved LSM configuration and public health evaluations were analyzed in addition to quantifying the optimal LSM and explaining the possible associated mechanisms. Using the China Water Statistical Yearbook for 2008−2017, data sets for the annual rainfall amounts (unit: mm), direct gross domestic product (GDP) loss caused by flood disasters, including floods (Tarabochia-Gast et al., 2022), landslides (Pollock & Wartman, 2020), and debris flows (unit: billion yuan), and flood-affected areas caused by flood disasters, including floods, landslides, and debris flows (unit: 10^3 ha) were collected for the YHRV region. These data sets were then used to determine the relationship between the annual rainfall and flood-affected GDP loss, and the relationship between the annual rainfall and flood-affected area. Finally, the effects of the precipitation simulation accuracies of different LSMs on the estimated GDP losses and flood-affected areas in the YHRV during the Meiyu in 2020 were evaluated by establishing appropriate relationships.

Figure 11a shows a scatter plot of the annual rainfall versus the GDP loss for the YHRV region from 2008 to 2017 as well as a fitted straight line. The fitted equation indicates that the GDP loss caused by flood disasters increased by about 51.33 billion yuan when the annual rainfall increased by 100 mm. Similarly, Figure 11b shows a scatter plot of the annual rainfall versus the flood-affected area for the YHRV region from 2008 to 2017 as well as a fitted straight line. When the annual rainfall increased by 100 mm, the flood-affected area increased by about 107.47 thousand hectares. Based on these proportional relationships, the errors in the GDP loss (flood-affected area) estimates among different LSMs for the Meiyu in YHRV during 2020 were solved and the results are shown in Figures 11c and 11d. The GDP loss overestimation ranged from 19.1 billion yuan with SSiB to 48.38 billion yuan with Pleim-Xiu, and the flood-affected area overestimation ranged from 19.10 thousand hectares with SSiB to 101.38 thousand hectares with Pleim-Xiu. Clearly, the flood disaster loss estimations differed greatly when different LSMs were used. Therefore, employing an accurate LSM can obtain more accurate precipitation forecasts and also reduce the uncertainties in flood disaster loss estimations.

5. Conclusions and Prospective

This study assessed the effectiveness of seven LSMs in WRFv4.3 precipitation simulations of the record-breaking Meiyu event in the YHRV region during 2020. The simulated period lasted 33 days from June 11 to July 13. A two-grid horizontally nested domain was used to simulate the Meiyu event in the YHRV region. The outer layer was the East China area with a spatial resolution of 27 km, and the inner layer was the YHRV region with a spatial resolution of 9 km. The uniform time step was 60 s.

Compared with the observations, the SSiB model obtained the best simulated daily precipitation results among the seven LSMs, followed by the Slab model and Pleim-Xiu. Evenly, it outperformed BMA result with seven LSMs.The proportion of ET relative to rainfall, surface heat flux, 850 hPa fields for the geopotential height and wind, and the moisture flux convergence were possible causes of the differences in the results simulated with the different LSMs. In addition, BMA was compared with the optimal scheme to demonstrate the superiority of the optimal LSM selected. Finally, the effects of the precipitation simulation accuracies of different LSMs on flood disaster loss estimation were also discussed to further demonstrate the superiority of the optimal LSM selected.
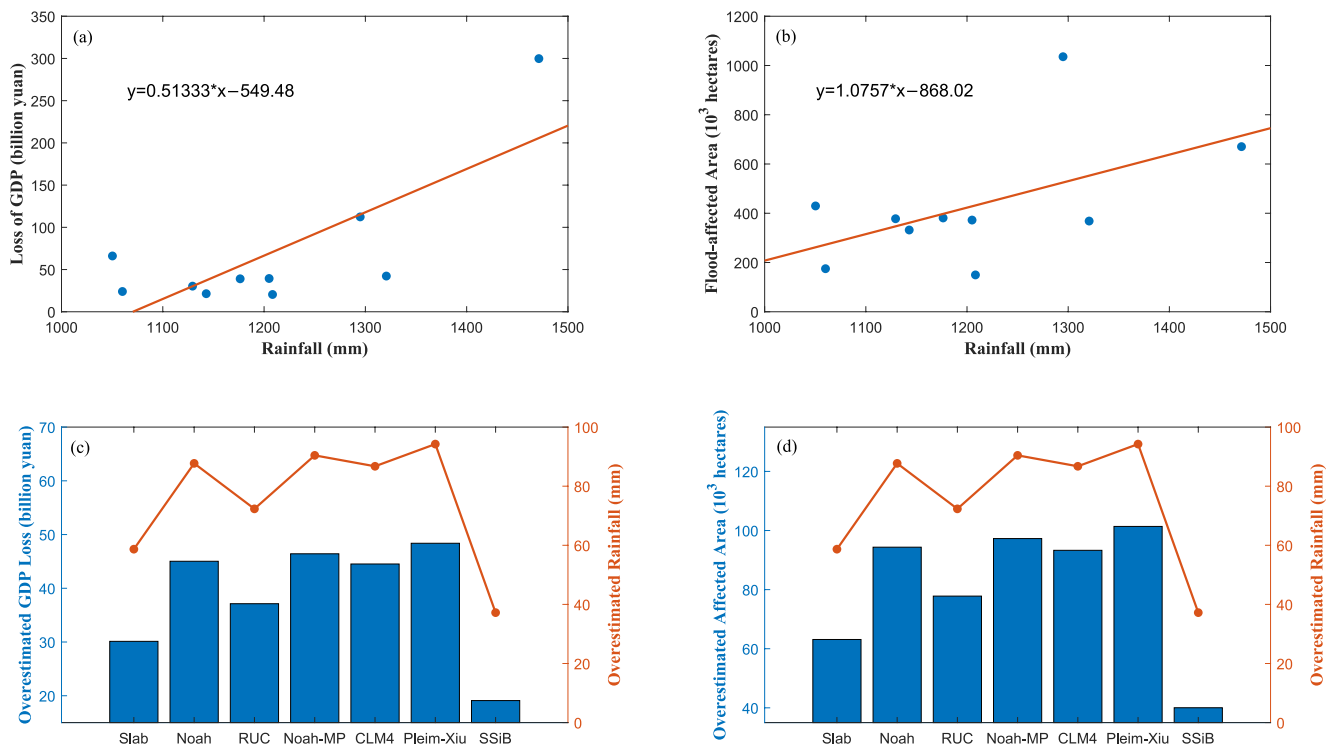
Figure 11. Relationships between rainfall amounts and flood disaster losses in the Yangtze–Huai river valley region. (a) Scatter plot of annual rainfall versus the GDP loss from 2008 to 2017 as well as a fitted straight line. (b) Scatter plot of annual rainfall versus the flood-affected area from 2008 to 2017 as well as a fitted straight line. (c) Overestimated GDP losses corresponding to overestimated rainfall amounts among different LSMs for the Meiyu in 2020. (d) Overestimated flood-affected areas corresponding to overestimated rainfall amounts among different LSMs for the Meiyu in 2020.

Many studies have evaluated the performance of different LSMs in WRF weather or climate simulations, but we considered some new LSMs and weather or climate events in a more comprehensive evaluation of the performance of LSMs in the WRF model. (a) We evaluated more LSMs by running the latest version of the WRF model. For example, all seven LSMs in WRF v4.3 were evaluated in this study and the results showed that the SSiB model performed best at precipitation simulation over the YHRV region in China. Most previous studies focused on evaluating the three LSMs comprising Noah, Noah-MP, and CLM4 in different regions throughout the world, but the SSiB model has not been considered widely despite its excellent performance. In addition, Pleim-Xiu and RUC have rarely been evaluated, and thus our findings may promote the use of these LSMs in future studies of land–atmosphere interactions. (b) We considered a representative precipitation event comprising the Meiyu season, which is a unique weather event in the East Asian monsoon region characterized by continuous precipitation. Many studies have investigated the formation and development of Meiyu events, and its relationship with tropical ocean signal, but few have assessed the effectiveness of different LSMs at simulating Meiyu events, especially the record-breaking Meiyu that occurred in June and July during 2020 in China.

However, it should be noted that selecting an optimal LSM can significantly reduce the simulation bias but model uncertainty still exists, and thus the constructed model may be defective and the parameters could be inaccurate in the current state. Therefore, future studies should focus on model development by refining the physical process descriptions (Zhou et al., 2018) as well as selecting and optimizing the critical physical parameters (Di et al., 2018, 2019; Duan et al., 2017) for the optimal LSM.

Conflict of Interest

The authors declare no conflicts of interest relevant to this study.

Data Availability Statement

The precipitation data sets used in our study can be freely accessed at https://www.ckcest.cn/default/es3/detail/4004/dw_dataset/C92AF495DE300001E327C1BD56401982. The data sets for the direct gross domestic product (GDP) losses and flood-affected areas can be obtained from the China Water Statistical Yearbook (https://sltjnj.digiwater.cn/index.htm?locale=zh_CN).

References

Attada, R., Kumar, P., & Dasari, H. P. (2018). Assessment of land surface models in a high-resolution atmospheric model during Indian summer monsoon. *Pure and Applied Geophysics*, *175*(10), 3671–3696. https://doi.org/10.1007/s00024-018-1868-z

Chen, F., & Dudhia, J. (2001). Coupling an advanced land surface-hydrology model with the Penn State-NCAR MM5 modeling system. Part I. Model implementation and sensitivity. *Monthly Weather Review*, *129*(4), 569–585. https://doi.org/10.1175/1520-0493(2001)129<0569:CAALSH>2.0.CO;2

Chen, F., Liu, C., Dudhia, J., & Chen, M. (2014). A sensitivity study of high-resolution regional climate simulations to three land surface models over the western United States. *Journal of Geophysical Research: Atmospheres*, *119*(12), 7271–7291. https://doi.org/10.1002/2014JD021827

Chen, X., Wen, Z., Song, Y., & Guo, Y. (2022). Causes of extreme 2020 Meiyu-Baiu rainfall: A study of combined effect of Indian Ocean and Arctic. *Climate Dynamics*, *59*(11–12), 3485–3501. https://doi.org/10.1007/s00382-022-06279-0

Constantinidou, K., Hadjinicolaou, P., Zittis, G., & Lelieveld, J. (2020). Performance of land surface schemes in the WRF model for climate simulations over the MENA-CORDEX domain. *Earth Systems and Environment*, *4*, 647–665. https://doi.org/10.1007/s41748-020-00187-1

Di, Z., Ao, J., Duan, Q., Wang, J., Gong, W., Shen, C., et al. (2019). Improving WRF model turbine-height wind-speed forecasting using a surrogate-based automatic optimization method. *Atmospheric Research*, *226*, 1–16. https://doi.org/10.1016/j.atmosres.2019.04.011

Di, Z., Duan, Q., Wang, C., Ye, A., Miao, C., & Gong, W. (2018). Assessing the applicability of WRF optimal parameters under the different precipitation simulations in the Greater Beijing Area. *Climate Dynamics*, *50*(5–6), 1927–1948. https://doi.org/10.1007/s00382-017-3729-3

Ding, Y., Liu, Y., & Hu, Z. (2021). The record-breaking Meiyu in 2020 and associated atmospheric circulation and tropical SST anomalies. *Advances in Atmospheric Sciences*, *38*(12), 1980–1993. https://doi.org/10.1007/s00376-021-0361-2

Duan, Q., Di, Z., Quan, J., Wang, C., Gong, W., Gan, Y., et al. (2017). Automatic model calibration-a new way to improve numerical weather forecasting. *Bulletin of the American Meteorological Society*, *98*(5), 959–970. https://doi.org/10.1175/BAMS-D-15-00104.1

Dudhia, J. (1996). A multi-layer soil temperature model for MM5. In *The sixth annual PSU/NCAR mesoscale model users' workshop*. PSU/NCAR.

Dudhia, J., Gill, D., Manning, K., Wang, W., & Bruyere, C. (1999). *PSU/NCAR mesoscale modeling system tutorial class notes and user's guide: MM5 modeling system version 3*. NCAR. https://doi.org/10.1016/S0924-0136(97)00397-X

Friend, A. D., & Kiang, N. Y. (2005). Land surface model development for the GISS GCM: Effects of improved canopy physiology on simulated climate. *Journal of Climate*, *18*(15), 2883–2902. https://doi.org/10.1175/JCLI3425.1

García-García, A., Cuesta-Valero, F. J., Beltrami, H., González-Rouco, J. F., & García-Bustamante, F. (2022). WRF v.3.9 sensitivity to land surface model and horizontal resolution changes over North America. *Geoscientific Model Development*, *15*(2), 413–428. https://doi.org/10.5194/gmd-15-413-2022

Hong, S. Y. (2010). A new stable boundary layer mixing scheme and its impact on the simulated East Asian summer monsoon. *Quarterly Journal of the Royal Meteorological Society*, *136*(651), 1481–1496. https://doi.org/10.1002/qj.665

Hong, S. Y., & Lim, J. O. J. (2006). The WRF single-moment 6-class microphysics scheme (WSM6). *Asia-Pacific Journal of Atmospheric Sciences*, *42*(2), 129–151.

Huang, X., Zhou, H., Yang, X., Zhou, W., Huang, J., & Yuan, Y. (2021). Spatial characteristics of coronavirus disease 2019 and their possible relationship with environmental and meteorological factors in Hubei province, China. *GeoHealth*, *5*(6), e2020GH000358. https://doi.org/10.1029/2020GH000358

Ji, L., Zhi, X., Zhu, S., & Fraedrich, K. (2019). Probabilistic precipitation forecasting over East Asia using Bayesian model averaging. *Monthly and Forecasting*, *34*(2), 377–392. https://doi.org/10.1175/WAF-D-18-0093.1

Kain, J. S. (2004). The Kain-Fritsch convective parametrization: An update. *Journal of Applied Meteorology and Climatology*, *43*(1), 170–181. https://doi.org/10.1175/1520-0450(2004)043<0170:TKCPAU>2.0.CO;2

Li, M., Di, Z., & Duan, Q. (2021). Effect of sensitivity analysis on parameter optimization: Case study based on streamflow simulations using the SWAT model in China. *Journal of Hydrology*, *603*, 126896. https://doi.org/10.1016/j.jhydrol.2021.126896

Li, M., Ma, Z., Gu, H., Yang, Q., & Zheng, Z. (2017). Production of a combined land surface data set and its use to assess land-atmosphere coupling in China. *Journal of Geophysical Research: Atmospheres*, *122*(2), 948–965. https://doi.org/10.1002/2016JD025511

Li, W., Guo, W., Xue, Y., Fu, C., & Qiu, B. (2016). Sensitivity of a regional climate model to land surface parameterization schemes for East Asian summer monsoon simulation. *Climate Dynamics*, *47*(7–8), 2293–2308. https://doi.org/10.1007/s00382-015-2964-8

Liu, J., Jia, B., Xie, Z., & Shi, C. (2016). Ensemble simulation of land evapotranspiration in China based on a multi-forcing and multi-model approach. *Advances in Atmospheric Sciences*, *33*(6), 673–684. https://doi.org/10.1007/s00376-016-5213-0

Liu, Y., & Ding, Y. (2020). Characteristics and possible causes for the extreme Meiyu in 2020. *Meteorological Monthly*, *46*(11), 1393–1404. https://doi.org/10.7519/j.issn.1000-0526.2020.11.001

Lu, S., & Zuo, H. (2021). Sensitivity of South Asian summer monsoon simulation to land surface schemes in weather research and forecasting model. *International Journal of Climatology*, *41*(15), 6805–6824. https://doi.org/10.1002/joc.7278

Manabe, S. (1969). Climate and the ocean circulation: I the atmospheric circulation and the hydrology of the Earth's surface. *Monthly Weather Review*, *97*(11), 739–774. https://doi.org/10.1175/1520-0493(1969)097<0739:CATOC>2.3.CO;2

Mlawer, E., Taubman, S. J., Brown, P. D., Iacono, M. J., & Clough, S. A. (1997). Radiative transfer for inhomogeneous atmospheres: RRTM, a validated correlated-k model for the longwave. *Journal of Geophysical Research*, *102*(D14), 16663–16682. https://doi.org/10.1029/97JD00237

Niu, G. Y., Yang, Z., Mitchell, K. E., Chen, F., Ek, M. B., Barlage, M., et al. (2011). The community Noah land surface model with multiparameterization options (Noah-MP): 1. Model description and evaluation with local-scale measurements. *Journal of Geophysical Research*, *116*(D12), D12109. https://doi.org/10.1029/2010JD015139

Oleson, K. W., Lawrence, D. M., Bonan, G. B., Flanner, M. G., Kluzek, E., Lawrence, P., et al. (2010). Technical description of version 4 of the community land model (CLM). NCAR tech. Note NCAR/TN-478+STR.

Pleim, J. E., & Xiu, A. (1995). Development and testing of a surface flux and planetary boundary layer model for application in mesoscale models. *Journal of Applied Meteorology and Climatology*, *34*(1), 16–32. https://doi.org/10.1175/1520-0450-34.1.16

Pollock, W., & Wartman, J. (2020). Human vulnerability to landslides. *GeoHealth*, *4*(10), e2020GH000287. https://doi.org/10.1029/2020GH000287

Pu, Z., & Kalnay, E. (2018). Numerical weather prediction basics: Models, numerical methods, and data assimilation. In Q. Duan, F. Pappenberger, J. Thielen, A. Wood, H. Cloke, & J. Schaake (Eds.), *Handbook of hydrometeorological ensemble forecasting*. Springer.

Qiao, S., Chen, D., Wang, B., Cheung, H., Liu, F., Cheng, J., et al. (2021). The longest 2020 Meiyu season over the past 60 years: Subseasonal perspective and its predictions. *Geophysical Research Letters*, *48*(9), 1–11. https://doi.org/10.1029/2021GL093596

Raftery, A. E., Gneiting, T., Balabdaoui, F., & Polakowski, M. (2005). Using Baysian model averaging to calibrate forecast ensembles. *Monthly Weather Review*, *133*(5), 1155–1174. https://doi.org/10.1175/MWR2906.1

Reddy, B. R., Srinivas, C. V., Shekhar, S. S. R., & Venkatraman, B. (2020). Impact of land surface physics in WRF on the simulation of sea breeze circulation over southeast coast of India. *Meteorology and Atmospheric Physics*, *132*(6), 925–943. https://doi.org/10.1007/s00703-020-00726-5

Shen, Y., Zhao, P., Pan, Y., & Yu, J. (2014). A high spatiotemporal gauge-satellite merged precipitation analysis over China. *Journal of Geophysical Research: Atmosphere*, *119*(6), 3063–3075. https://doi.org/10.1002/2013JD020686

Shirvani, A., Fadaei, A. S., & Landman, W. A. (2019). The linkage between geopotential height and monthly precipitation in Iran. *Theoretical and Applied Climatology*, *136*(1–2), 221–236. https://doi.org/10.1007/s00704-018-2479-4

Skamarock, W. C., Klemp, J. B., Dudhia, J., Gill, D. O., Liu, Z., Berner, J., et al. (2021). A description of the advanced research WRF model version 4.3. No. NCAR/TN-556+STR. https://doi.org/10.5065/1dfh-6p97

Smirnova, T. G., Brown, J. M., Benjamin, S. G., & Kenyon, J. S. (2016). Modifications to the rapid update cycle land surface model (RUC LSM) available in the weather research and forecasting (WRF) model. *Monthly Weather Review*, *144*(5), 1851–1865. https://doi.org/10.1175/MWR-D-15-0198.1

Tarabochia-Gast, A. T., Michanowicz, D. R., & Bernstein, A. S. (2022). Flood risk to hospitals on the United States Atlantic and Gulf Coasts from hurricanes and sea level rise. *GeoHealth*, *6*(10), e2022GH000651. https://doi.org/10.1029/2022GH000651

Tsuji, H., Takayabu, Y. N., Shibuya, R., Kamahori, H., & Yokoyama, C. (2021). The role of free-tropospheric moisture convergence for summertime heavy rainfall in Western Japan. *Geophysical Research Letters*, *48*(18), e2021GL095030. https://doi.org/10.1029/2021gl095030

van den Hurk, B., Kim, H., Krinner, G., Seneviratne, S. I., Derksen, C., Oki, T., et al. (2016). LS3MIP (v1.0) contribution to CMIP6: The land surface, snow and soil moisture model intercomparison project—Aims, setup and expected outcome. *Geoscientific Model Development*, *9*(8), 2809–2832. https://doi.org/10.5194/gmd-9-2809-2016

Wang, M., Zeng, X., Wang, N., Yi, X., Zhou, X., & Wang, B. (2016). Sensitivity of simulated summer temperature and precipitation to land surface schemes by WRF. *Meteorology and Disaster Reduction Research*, *39*(1), 32–40. (in Chinese). https://doi.org/10.12013/qxyjzyj2016-004

Wu, Y., Miao, C., Sun, Y., AghaKouchak, A., Shen, C., & Fan, X. (2021). Global observations and CMIP6 simulations of compound extremes of monthly temperature and precipitation. *GeoHealth*, *5*(5), e2021GH000390. https://doi.org/10.1029/2021GH00039

Xiao, Y., Ma, Z., & Li, M. (2017). Evaluation of the parameterizations of soil moisture influence on evapotranspiration in land surface models. *Chinese Journal of Atmospheric Sciences*, *41*(1), 132–146. (in Chinese). https://doi.org/10.3878/j.issn.1006-9895.1606.1529

Xinhua NEWs. (2020). Over 54.8 MLN people affected by floods in China. Archived from Retrieved from http://www.xinhuanet.com/english/2020-07/29/c_139247084.htm

Xue, Y., Sellers, P. J., Kinter, J. L., & Shukla, J. (1991). A simplified biosphere model for global climate studies. *Journal of Climate*, *4*(3), 345–364. https://doi.org/10.1175/1520-0442(1991)004<0345:ASBMFG>2.0.CO;2

Yan, Y., Tang, J., Wang, S., Niu, X., & Wang, L. (2021). Uncertainty of land surface model and land use data on WRF model simulations over China. *Climate Dynamics*, *57*(7–8), 1833–1851. https://doi.org/10.1007/s00382-021-05778-w

Yuan, X., Xie, Z., Zheng, J., Tian, X., & Yang, Z. (2008). Effects of water table dynamics on regional climate: A case study over East Asian monsoon area. *Journal of Geophysical Research*, *113*(D21), D21112. https://doi.org/10.1029/2008JD010180

Zeng, X., Wu, Z., & Song, S. (2012). Effects of land surface schemes on the simulation of a heavy rainfall event by WRF. *Chinese Journal of Geophysics*, *55*, 16–28. (in Chinese). https://doi.org/10.6038/j.issn.0001-5733.2012.01.002

Zeng, X., Wu, Z., Xiong, S., Song, S., Zheng, Y., & Liu, H. (2011). Sensitivity of simulated short-range high-temperature weather to land surface schemes by WRF. *Science China Earth Sciences*, *54*(4), 581–590. https://doi.org/10.1007/s11430-011-4181-6

Zhang, C., Di, Z., Duan, Q., Xie, Z., & Gong, W. (2020). Improved land evapotranspiration simulation of the community land model using a surrogate-based automatic parameter optimization method. *Water*, *12*(4), 943. https://doi.org/10.3390/w12040943

Zhong, L., Huang, Z., Ma, Y., Fu, Y., Chen, M., Ma, M., & Zheng, J. (2021). Assessments of weather research and forecasting land surface models in precipitation simulation over the Tibetan Plateau. *Earth and Space Science*, *8*(3), e2020EA00156. https://doi.org/10.1029/2020EA001565

Zhong, S., Yang, S., & Chen, Z. (2019). Evaluation of the parameterization schemes and nudging techniques in GRAPES for warm sector torrential rains using surface observations. *Journal of Tropical Meteorology*, *25*(3), 353–364. https://doi.org/10.16555/j.1006-8775.2019.03.007

Zhou, X., Yang, K., & Wang, Y. (2018). Implementation of a turbulent orographic form drag scheme in WRF and its application to the Tibetan Plateau. *Climate Dynamics*, *50*(7–8), 2443–2455. https://doi.org/10.1007/s00382-017-3677-y

Zhuo, L., Dai, Q., Han, D., Chen, N., & Zhao, B. (2019). Assessment of simulated soil moisture from WRF Noah, Noah-MP, and CLM land surface schemes for landslide hazard application. *Hydrology and Earth System Sciences*, *23*(10), 4199–4218. https://doi.org/10.5194/hess-23-4199-2019